Rotating Velocimetry Based Upon Rotational Doppler Effect of Perfect Laguerre–Gaussian Light Modes

Yanxiang Zhang, Zijing Zhang, Zhongquan Nie, and Yuan Zhao

***Abstract*— Laser Doppler rotational velocimetry has emerged as a pivotal technology for astronomical survey and remote sensing. While high-order optical vortices are commonly used for accurate rotating velocimetry, their large annular radii can pose a challenge when detecting a small cross-sectional rotator directly. Here, we overcome this limitation by exploiting perfect Laguerre–Gaussian (PLG) light modes carrying orbital angular momentum, based upon the rotational Doppler effect. In this situation, the beating frequency signals can be observed as well, regardless of the rotator being exposed to the symmetrically or asymmetrically superposed PLG light modes, thus revealing the linked rotating velocity. What is more, a direct proof-of-principle experiment is conducted to validate the performance of the velocimetry system. It shows that ±15-order modes provide the optimal sensitivity of detecting rotating velocity, corresponding to a relative uncertainty of below 0.48%. In contrast to the existing techniques, our rotating velocimetry platform not only enables small target detection, but also offers a tunable flexibility together with a higher velocimetry accuracy. Hence, this indicates the generation of a high-accuracy rotating velocimetry pathway by resorting to the perfect structured vortex light modes. Such validated findings might be useful for practical optical metrology and remote sensing scenarios.**

***Index Terms*— Detection accuracy, orbital angular momentum (OAM), perfect Laguerre–Gaussian (PLG) light, rotational velocimetry.**

I. Introduction

THE ever-growing demands of higher sensitivity and accuracy in laser remote sensing systems require the optimization of metrological signals to achieve the highest possible signal-to-noise ratio (SNR) or the lowest permissible error [1]. Driven by its applicability, the classical linear Doppler effect has aroused considerable attentions in the fields of optics, electronics, and magnetism [2], [3], [4], thus giving rise to widespread developments and practical applications on fluid aerodynamics as well as object monitoring and control [5], [6], etc. However, such traditional nonrelativistic Doppler protocol restricts the direct observable velocity to only the longitudinal velocity component. To tackle this restriction, researchers have demonstrated the feasibility of exploiting the orbital-angular-momentum (OAM)-dependent rotational Doppler effect to measure transverse rotating velocity, which has not only breathed a new life into the area of the laser velocimetry, but also refreshed our understanding of real-world remote detection scenarios [7], [8], [9], [10], [11], [12], [13]. Up until now, a myriad of rotating velocimetry schemes based on the optical rotational Doppler effect has been developed. These embraces emit various OAM-carrying structured light modes to validate the relation between rotational Doppler shift (RDS) and rotating velocity [14], [15], [16], analyzing relative deviation cases of the rotary shaft and light axis [17], [18] as well as taking the advantage of the nonzero radial index to improve the SNR of rotational Doppler signals [19].

In general, in order to saliently improve the precision of rotating velocimetry, selecting an OAM light mode with a large topological charge (TC) or OAM index within the allowed system bandwidth is an efficient strategy. This allows for the detected RDSs containing motion messages to be validly amplified [20]. However, as the spatial mode radius is dependent on the TC, the validly illuminated or scattered cross-sectional areas of a small target sharply shrink with the increased ring size. This causes the detectable Doppler signals to lose effectiveness when detecting a smaller target. The perfect optical vortex (POV), credited to Ostrovsky et al. [21], might be able to alleviate such onrushing technical challenge to some extent since the beam radius is immune to the variations of the TC. As such, Qiu et al. [22] wisely introduced this beam to realize rotational Doppler velocity detections, validating its feasibility and showing the same well detection performance in comparison to Laguerre–Gaussian (LG) modes. Apart from that, less well-known is the novel perfect Laguerre–Gaussian (PLG) mode, recently presented theoretically by Mendoza-Hernández et al. [23], which possesses the parallel perfect character as the POV. After then, such scalar modes together with their vectorial counterparts have also been experimentally measured by Liu et al. [24]. Although the PLG modes possess the parallel perfect feature,

Manuscript received 3 January 2023; revised 21 April 2023; accepted 6 May 2023. Date of publication 1 August 2023; date of current version 7 August 2023. This work was supported in part by the National Natural Science Foundation of China under Grant 62075049, Grant 11974258, and Grant 11604236; in part by the Key Research and Development (R&D) Projects of Shanxi Province under Grant 201903D121127; and in part by the Science and Technology Foundation of Guizhou Province under Grant ZK [2021]031. The Associate Editor coordinating the review process was Dr. Shiraz Sohail. *(Corresponding authors: Zijing Zhang; Zhongquan Nie.)*

Yanxiang Zhang, Zijing Zhang, and Yuan Zhao are with the Department of Physics, Harbin Institute of Technology, Harbin 150001, China (e-mail: zhangyanxiang@hit.edu.cn; zhangzijing@hit.edu.cn; zhaoyuan@hit.edu.cn).

Zhongquan Nie is with the Key Laboratory of Advanced Transducers and Intelligent Control System, Ministry of Education and Shanxi Province, College of Physics and Optoelectronics, Taiyuan University of Technology, Taiyuan 030024, China (e-mail: niezhongquan1018@163.com).

Digital Object Identifier 10.1109/TIM.2023.3277933

the feasibility of rotational Doppler velocimetry by exploiting such specific beams remains to be elusive thus far, hindering the high-accuracy velocimetry of a rotating target with a small cross section.

In these contexts, we here theoretically propose and experimentally demonstrate a high-accuracy measurement scheme for the rotating angular velocimetry, by exploiting the novel PLG light mode along with the rotational Doppler effect. We start with the theoretical study on the intensity, phase, and perfect properties of PLG modes, and highlight the perfect benefit to achieve velocimetry of a rotating target with a small cross section. Then, the mechanism of rotational Doppler velocimetry is examined. Subsequently, a proof-of-concept experiment is implemented and the experimental results demonstrate that in addition to symmetrically superimposed PLG modes, the asymmetrically superimposed equivalents impinging onto the small rotating target can also induce scattered beating frequency. The experimental outcomes validate our theoretical predictions well. Crucially, we further show how to quantitatively evaluate the salient performances of the rotational Doppler velocimetry system. Lastly, we draw our conclusions.

II. Theoretical Framework

A. PLG Modes

Here, we first present the theoretical formula of PLG modes. The complex amplitude expression of PLG modes at $z = 0$ can be formulated as [23], [24], [25]

$$E_l(r, \varphi, z) = \left(\frac{\sqrt{2}\, r}{w_l}\right)^{|l|} L_p^{|l|}\left(\frac{2r^2}{w_l^2}\right) \exp\left(-\frac{r^2}{w_l^2}\right) \exp(il\varphi)\mathbf{e}_x \tag{1}$$

where (r, φ, z) denotes the cylindrical coordinates, meeting the relation with the Cartesian coordinates (x, y, z) as $r = (x^2 + y^2)^{1/2}$ and $\varphi = \arctan(y/x)$. $L_p^{|l|}(\bullet)$ stands for the Laguerre polynomial with the radial mode index p, as well as the OAM mode index l. $\mathbf{e}_x$ represents the light's polarization state along the x-direction. As reported in [23], [24], and [25], the beam waist w_l of the PLG modes can be given by

$$w_l \equiv \frac{w_0}{2\sqrt{2p + |l| + 1}}. \tag{2}$$

Here, w_0 is the beam waist of an LG mode. Thus, the intensity of PLG modes following (1) can be represented as:

$$I(r, \varphi, z) = E_l(r, \varphi, z) \cdot E_l^*(r, \varphi, z) = |E(r, \varphi, z)|^2. \tag{3}$$

Fig. 1(a) and (b) shows the simulated intensity and phase distributions of the PLG modes with OAM index $l = 10$ as an example, respectively. From Fig. 1(a), the transverse intensity with an overlapped cross-sectional profile presents a single ring-shaped intensity structure. The azimuthal phase factor $\exp(il\varphi)$ in (1) indicates that the phase distribution of the PLG mode exhibits a spiral phase front, as shown in Fig. 1(b). It is clear that the total phase step from 0 to 2π around the center equals to l. Moreover, in order to validate the fidelity of the proposed light fields, the corresponding 3-D iso-intensity surface profile is depicted in Fig. 1(c), which displays

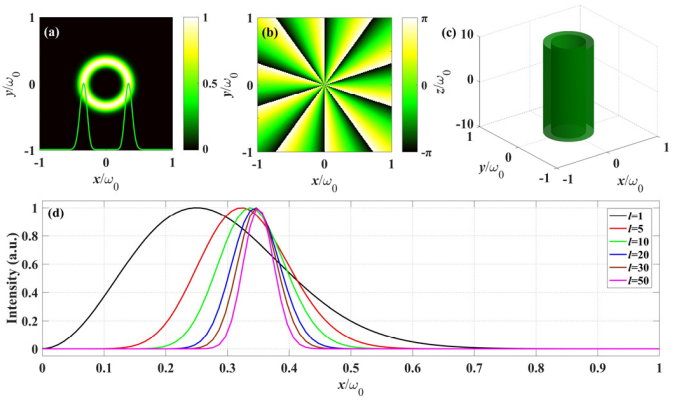

Fig. 1. Schematic of PLG modes at $z = 0$ plane: (a) transverse intensity pattern with $p = 0$ and $l = 10$ overlapped with the cross-sectional profile (green solid line) and (b) its phase distribution; (c) corresponding 3-D iso-intensity surface profile; and (d) cross-sectional intensity with the varied l from 1 to 50, charactering the perfect property of PLG light modes. The simulated parameters throughout this article are selected as follows. The laser beams with a center wavelength of $\lambda = 532$ nm and the beam size $w_0 = 2$ mm.

good consistency with that in Fig. 1(a). Furthermore, Fig. 1(d) illustrates the cross-sectional intensity profiles with l varying from 1 to 50. It can be found that the ring thickness, which is considered as the full-width at half-maximum of each profile, decreases with the increase of l. The ring radius, defined as the distance of optical axis and the position of the strongest intensity, gradually tends to be constant as the l enlarges, thus illustrating a perfect feature. It is worth noting in Fig. 1(d) that there is a large shift while going from $l = 1$ to $l = 5$. This can be ascribed to the contribution of the term $(\sqrt{2}\, r/w_l)^{|l|}$ in (1) that results in the increased hollow dark-core region with enlarged l, thus causing the gradually increased bright ring radius. In addition, the cross-sectional intensity profile becomes sharp except for $l = 1$, which is because the increased dark-core region with higher values of l gives rise to the reduction in the ring thickness. Such perfect OAM modes might be conducive to detecting rotating velocity of a target with small cross sections, while maintaining high detected accuracy with the increased l.

B. Rotational Doppler Velocimetry

Having elaborated on the perfect benefit of the proposed PLG modes, we proceed to the analyses of the related rotational Doppler velocimetry. In practical detection processes, as the light frequency is typically too higher than the resultant Doppler shifts to detect them directly, a coherent detection method is adopted to acquire the Doppler echo signals. The interferometric modes consist of two superposed PLG modes with OAM indices l_1 and l_2, and can be expressed as

$$E(r, \varphi, z) = E_{l_1}(r, \varphi, z) + E_{l_2}(r, \varphi, z). \tag{4}$$

During the detection process, we normally guide such interferometric modes onto a rough-surfaced rotating target with a rotating velocity Ω. As a consequence, the motion induces the RDS in backscattered echo light signals. On the probe end, since the detector can merely capture the intensity information, we need to calculate the modulus square of (4),

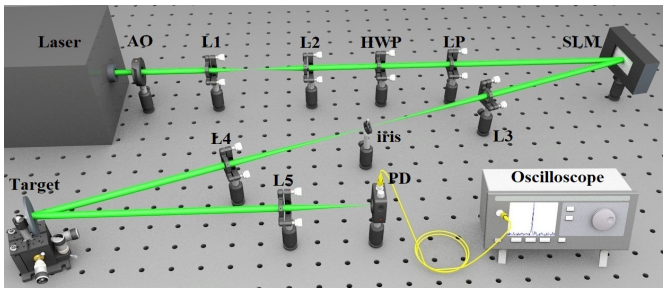

Fig. 2. Experimental setup for the generation of arbitrary spatial light modes as well as the measurement of the rotational velocity of a rotor. OA: optical attenuator; L1–L5: lenses; HWP: half-wave plate; LP: linear polarizer; SLM: spatial light modulator; and PD: photodetector.

to obtain the time-varying intensity signals $I(t)$, which can be given as

$$\begin{aligned} I(t) &= |E(r,\varphi,z)|^2 \\ &\propto |\exp(il_1\varphi)+\exp(il_1\varphi)|^2 \\ &= \left|\exp\left(i\frac{l_1+l_2}{2}\varphi\right)\left[\exp\left(i\frac{l_1-l_2}{2}\varphi\right)+\exp\left(i\frac{l_1-l_2}{2}\varphi\right)\right]\right|^2 \\ &\propto |1+\cos[(l_1-l_2)\Omega t]|. \end{aligned} \tag{5}$$

To acquire the RDS, it is requisite to perform the fast Fourier transform (FFT) to the time-varying intensity signals in (5). After this, in the transformed power spectra, we can extract the RDS by taking the deviation of the phase term in (5)

$$\Delta f = \left|\frac{\mathrm{d}[(l_1-l_2)\Omega t]}{2\pi\,\mathrm{d}t}\right| = \frac{|l_1-l_2|\Omega}{2\pi}. \tag{6}$$

Hence, the desired rotating velocity can be inferred as $\Omega = 2\pi\Delta f/|l_1-l_2|$. In (6), it is clear that the beating frequency can be obtained by the combination of two OAM light fields with OAM indices l_1 and l_2.

III. Experimental Methodology

To demonstrate the effectivity of our proposed scheme, a proof-of-principle experiment is conduced, and the compact and robust experimental setup is illustrated in Fig. 2. First, a Gaussian light beam emitted from a diode-pumped solid-state laser with a wavelength of 532 nm is appropriately attenuated by an optical attenuator (OA). After then, the beam is collimated and expanded with a telescope configuration consisting of two lenses (L1 and L2), respectively. To control the emitted power and polarization, a half-wavelength plate and a linear polarizer (LP) are used in conjunction. Before the beams are guided onto a reflective phase-only spatial light modulator (SLM), the LP is rotated to match the polarization requirements of the SLM. To create the desired PLG modes and its interferometric equivalents by virtue of the available SLM, the predesigned digital holograms are loaded upon the SLM panel. We here adopt to a versatile complex-amplitude-modulated technology to engineer the digital holograms [26], [27], and the relevant transmissive function can

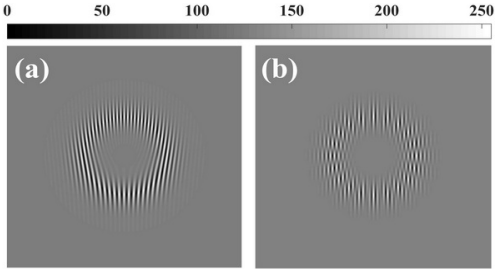

Fig. 3. Digital holograms: (a) PLG mode with OAM index of $l = 10$ and (b) PLG interferometric mode with OAM indices of $l_1 = -l_2 = 10$. The gray levels of these images range from 0 to 255.

be represented as follows:

$$\begin{aligned} &T(x,y) \\ &= \mathrm{mod}\left\{F\left[A(x,y)\right]\sin\left[\varphi(x,y)+2\pi\left(f_x x+f_y y\right)\right],2\pi\right\} \end{aligned} \tag{7}$$

where $\mathrm{mod}\{\bullet\}$ denotes the modulus function. $A(x, y)$ and $\varphi(x, y)$ are, respectively, the amplitude and phase of incident optical modes. f_x and f_y depict the grating frequencies along the horizontal and vertical directions, respectively. Fig. 3 shows the exemplary digital holograms concerning both the specific PLG mode and its interferometric one, respectively. Subsequently, the generated optical modes pass through a $4f$ system, consisting of two identical lenses (L3 and L4) and a tunable iris located in the Fourier plane, before relaying the images to the far field. Notably, a charge-coupled device (CCD) detector (not shown here) positioned behind the L4 is employed to detect the generated optical modes.

To achieve the rotating velocimetry, we directly guide the generated PLG interferometric modes onto an electromotive rotating target surface vertically, where the target is mounted on a 3-D stage. We then detect the scattered echo light signals by a receive system including a collection lens (L5) and a photodetector (PD). An oscilloscope connected with this PD is utilized to digitalize the modulated time-varying analog signals. We then gather the signals and perform their FFT on a personal computer. Ultimately, the RDS can be extracted via searching for frequency spectrum peaks in transformed power spectra, thus easily inferring the rotating velocity.

IV. Experimental Results and Discussion

In this section, we first examine several different PLG interferometric modes. Fig. 4 shows, in turn, the simulated phase textures [Fig. 4(a)–(d)], and the simulated and experimental PLG interferometric modes [Fig. 4(e)–(l)], with four distinct OAM indices of $l_1 = 15$ and $l_2 = 10$, $l_1 = -l_2 = 10$, $l_1 = 15$, and $l_2 = -10$, as well as $l_1 = -l_2 = 15$. Unambiguously, it can be observed from Fig. 4(e)–(h) that all of the field modes feature petal-like structures, in which the petal numbers are equal to $|l_1 - l_2|$. The generation of these petal textures is due to the fact that $[\exp(il_1\varphi) + \exp(-il_1\varphi)]^2 \propto \cos(|l_1 - l_2|\varphi)$, thus leading to the alternation between bright and dark lobes along the azimuthal direction, where $\exp(il\varphi)$ is equivalently the OAM eigenfunction with eigenvalues of l. In these regards,

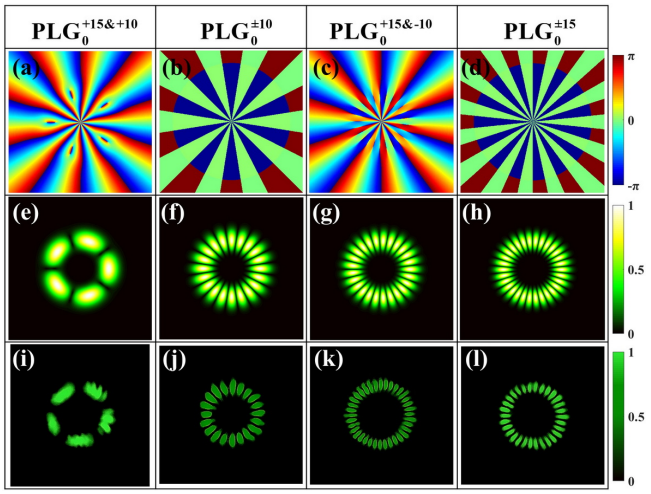

Fig. 4. PLG interferometric modes with the radial index $p = 0$ and the OAM indices: $l_1 = 15$ and $l_2 = 10$, $l_1 = 10$ and $l_2 = -10$, $l_1 = 15$ and $l_2 = -10$, and $l_1 = 15$ and $l_2 = -15$, respectively: (a)–(d) calculated phase textures; (e)–(h) simulated intensity patterns; and (i)–(l) experimental intensity distributions.

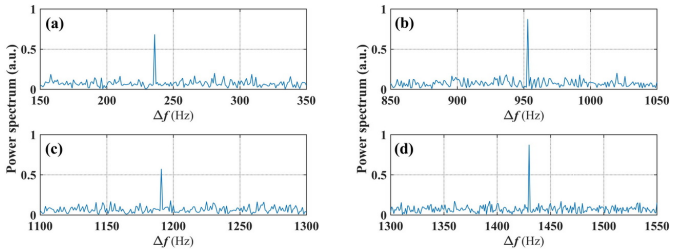

Fig. 5. Experimentally measured power spectra as a function of RDS, corresponding to illuminated PLG interferometric light modes with distinct OAM indices: (a) 15 and 10; (b) ±10; (c) 15 and −10; and (d) ±15. The rotational velocity is fixed at 300 rad/s.

it can be seen that the experimental outcomes in Fig. 4(i)–(l) are in a good agreement with the simulated counterparts.

Then, the rotating velocity of the prescribed target is fixed at 300 rad/s, and the power spectra under the illumination of different PLG interferometric modes are measured as shown in Fig. 4(i)–(l). The measured results are shown in Fig. 5, where each power spectrum is normalized to the maximum value. It can be clearly observed from Fig. 5 that there exists a clear signal peak in each power spectrum, which corresponds to the desired Doppler shift. Under such a circumstance, we are able to obtain the rotating velocity following (6). It is worth mentioning that in addition to the symmetrically superimposed PLG modes [Fig. 5(b) and (d)], the illuminated rotating target can also trigger rotational Doppler peak from the asymmetrically superimposed ones proposed in our scheme, as shown in Fig. 5(a) and (c). Furthermore, the RDSs can be read out from Fig. 5(a)–(d), equaling to 236, 953, 1191, and 1430 Hz, successively. As a result, the associated rotating velocity can be inferred as 296.56, 299.39, 299.33, and 299.49 rad/s, respectively. In fact, it should be noticed that the measured rotating velocities are all in close proximity to the default value of 300 rad/s, thus indicating that the OAM-carried PLG modes could view as a well-defined candidate for testing the rotating velocity with a high accuracy.

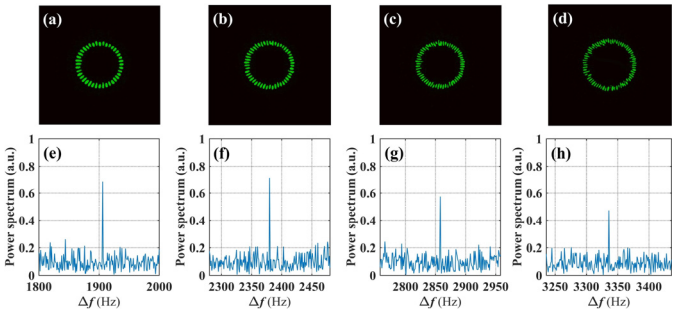

Fig. 6. Experimentally validating the perfect benefit of PLG light modes for rotating velocimetry of a target with small cross sections. The PLG interferometric modes with OAM indices: (a) ±20; (b) ±25; (c) ±30; (d) ±35; and (e)–(h) corresponding observed rotational Doppler spectra.

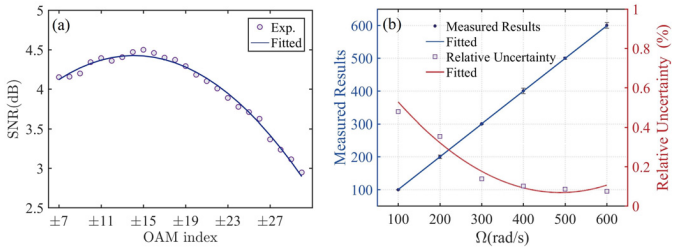

Fig. 7. Performance estimations with respect to the rotating Doppler velocimetry system: (a) measured SNR as a function of varied OAM indices with values from $l_1 = -l_2 = 7$–30 and (b) dependence of measured relative uncertainty on altering rotating velocity.

To further validate the presented perfect benefit for the rotating velocimetry, we next to increase the OAM indices of PLG interferometric modes from $l_1 = -l_2 = 20$, 25, 30–35, respectively. Fig. 6(a)–(h) shows the corresponding PLG interferometric light field patterns and the power spectra, respectively. In particular, it is found that the related power spectra display salient descending trends with the increased OAM indices. Nevertheless, clear Doppler peaks emerge in each measured spectrum, which means that the rotating velocity can also be acquired. Intriguingly, the radii of the petals in such measured processes are immune to the enlargement of OAM indices, thus validating the ability of remotely measuring rotating velocity of a given target with a small cross section.

Additionally, it is of vital significance to estimate the performance of our rotating velocimetry measurement system. To this end, we first measure the SNR as a function of PLG interferometric modes with varied OAM indices from $l_1 = -l_2 = 7$–30, to cherry-pick the optimal OAM index in the rotating velocimetry system. Here, the SNR can be defined as the ratio of the maximum signal peak with the maximum noise peak. The measured outcomes are shown in Fig. 7(a), where each data point is repeatedly measured 20 times, and the mean is regarded as the final measured result. It can be observed from Fig. 7(a) that the OAM index of $l_1 = -l_2 = 15$ shows the maximum SNR, which corresponds to the optimal sensitivity with respect to our proposed rotating velocimetry system. This might be understood as that the interferometric light field patterns corresponding to this OAM index reach a balance between OAM modal purity and moving away from the low-frequency noises domains, resulting in the highest SNR compared to lower or higher OAM indices. We further assess the performance of the rotating velocimetry

TABLE I
COMPARISONS OF THREE ASPECTS WHEN EMITTING DISTINCT OAM-CARRIED OPTICAL MODES, INCLUDING APPLICABLE TARGET CROSS SECTIONS, SETUP TUNABILITY, AND RELATIVE UNCERTAINTY

OAM-carried optical modes	Applicable target cross sections	Setup tunability	Relative uncertainty (%)	References
LG	large	high	1.3	[11]
White light	large	high	1.9	[12]
BG	large	high	–	[13]
Incoherent light	large	high	1	[14]
Ring airy Gaussian vortex	large	high	0.5	[9]
Perfect optical vortex	small	relatively low	1.4	[20]
PLG	small	high	0.48	This work

system via measuring the dependence of relative uncertainty on distinct rotating velocities in the case of optimal sensitivity ($l_1 = -l_2 = 15$). More specifically, we repeatedly measure each of the rotating velocity up to 50 times, when altering the set rotating velocity from 100 to 600 rad/s with the interval of 100 rad/s. Again, the means of each set of data are considered as the measured results, while the standard deviations are matched to the measured standard uncertainty denoted as error bars, as plotted in Fig. 7(b). The relative uncertainty can be defined as the ratio between the standard uncertainty and the mean of measured 50 times data. It is observed from Fig. 7(b) that the maximum relative uncertainty is below 0.48%, thus showing the high accuracy of our rotating velocimetry system.

In order to give a powerful insight into the demonstrated merits in this work, we further compare three pivotal indicators concerning the rotating velocimetry system for distinct OAM-carried optical modes: applicable target cross sections, setup tunability, and relative uncertainty, as shown in Table I. Even though exploiting the illumination of either coherent or incoherent light modes takes on the high tunability in the experimental setups, the detect objects are limited to large scales accompanying with the relative uncertainty of over 1% [9], [11], [12], [13], [14]. On the contrary, it has been proven that the use of POV is beneficial to detecting a small-cross-sectional target. Yet, an additional lens is required to implement the Fourier transform in the experiment, thus causing the relatively poor setup tunability [20]. This work, on the whole, unifies all the advantages of previous related research, namely, small-scale-target detection, flexibly tunable experimental setup, and extremely high measure accuracy. This totally indicates that this work offers a favorable platform for the velocity detection of small-cross-sectional targets with prominent tunability and high accuracy.

It is worth mentioning that the performance of the velocity detection system is almost insensitive to variations in rotating velocity $\mathbf{\Omega}$. Therefore, our comparisons do not depend on the specific value of $\mathbf{\Omega}$. While it is true that comparisons with other reported works may not be completely direct due to differences in experimental setups and conditions, we believe that our approach provides a novel and effective solution to the challenge of rotating velocity detection of small-cross-sectional targets, which has the potential to inspire and inform further developments in this area.

Additionally, our proposed scheme may have several limitations. First, the measurement scheme can only determine the magnitude of the rotating speed, while the rotating velocity vector, which includes the magnitude and direction information, cannot be detected simultaneously. This is because the absolute value of the RDS in (6) is taken. Second, it is essential to the optical axis of emitted PLG mode to be normally aligned with the rotary axis of the spinning object. Even a slight misalignment can cause the broadening of the OAM spectrum, thus leading to additional confused Doppler signal peaks. Lastly, in practical applications, the proposed method can be affected by the strong atmospheric turbulence, which can introduce measurement uncertainties. We plan to investigate this further in future studies to improve the accuracy and reliability of our method. In terms of perspectives, we believe that our proposed method has the potential to be applied in various fields, such as remote sensing, navigation, and robotics, where high-precision measurement of rotation speed is required.

V. CONCLUSION

To conclude, we have theoretically presented and experimentally demonstrated a high-accuracy rotating velocimetry paradigm, based upon the rotational Doppler effect of vortex-encoded PLG interferometric modes. First, we validate that the perfect property of optical modes can be used to determine unambiguously rotating velocity of a prescribed target with a small cross section. Otherwise, it is noteworthy that in addition to the symmetrically superimposed PLG modes, the asymmetrically counterparts impinging onto the rotating target can trigger the rotational Doppler signals as well. As a result, the rotating velocity can be ascertained correspondingly. More significantly, our experimental outcomes unveil that ± 15-order PLG interferometric modes offer the optimal rotating velocimetry sensitivity, while maintaining the relative uncertainty of below 0.48%. Our rotating velocimetry system possesses the advantages, in addition to being applicable to a small target detection, manifesting the flexible tunability while remaining a higher velocimetry accuracy than other paralleled methods. It is highly expected that the demonstrated protocol and findings would not only contribute to the study of OAM [28], [29], [30] and the interaction between photons and macroscopic object [31], but also pave the roadmap to extensive applications in laser Doppler velocimetry systems, remote sensing, and optical metrology [32], [33].

REFERENCES

[1] A. V. Jelalian, *Laser Radar Systems*. Boston, MA, USA: Artech House, 1992.

[2] H. Lin and K. Ding, "A new method for measuring engine rotational speed based on the vibration and discrete spectrum correction technique," *Measurement*, vol. 46, no. 7, pp. 2056–2064, Aug. 2013.

[3] J. Urbanek, T. Barszcz, and J. Antoni, "A two-step procedure for estimation of instantaneous rotational speed with large fluctuations," *Mech. Syst. Signal Process.*, vol. 38, no. 1, pp. 96–102, Jul. 2013.

[4] L. Wang, Y. Yan, Y. Hu, and X. Qian, "Rotational speed measurement through electrostatic sensing and correlation signal processing," *IEEE Trans. Instrum. Meas.*, vol. 63, no. 5, pp. 1190–1199, May 2014.

[5] M. F. Gard, "Optical measurement of angular deformation and torque inside a working drillstring," *IEEE Trans. Instrum. Meas.*, vol. 65, no. 8, pp. 1895–1901, Aug. 2016.

[6] M. Harris, R. I. Young, F. Köpp, A. Dolfi, and J.-P. Cariou, "Wake vortex detection and monitoring," *Aerosp. Sci. Technol.*, vol. 6, no. 5, pp. 325–331, Sep. 2002.

[7] A. Belmonte and J. P. Torres, "Optical Doppler shift with structured light," *Opt. Lett.*, vol. 36, no. 22, pp. 4437–4439, 2011.

[8] J. Courtial, K. Dholakia, D. A. Robertson, L. Allen, and M. J. Padgett, "Measurement of the rotational frequency shift imparted to a rotating light beam possessing orbital angular momentum," *Phys. Rev. Lett.*, vol. 80, no. 15, pp. 3217–3219, Apr. 1998.

[9] S. Qiu et al., "Observation of the rotational Doppler shift of the ring airy Gaussian vortex beam," *Opt. Commun.*, vol. 490, Jul. 2021, Art. no. 126900.

[10] L. Fang, M. J. Padgett, and J. Wang, "Sharing a common origin between the rotational and linear Doppler effects," *Laser Photon. Rev.*, vol. 11, no. 6, Nov. 2017, Art. no. 1700183.

[11] M. P. Lavery, F. C. Speirits, S. M. Barnett, and M. J. Padgett, "Detection of a spinning object using light's orbital angular momentum," *Science*, vol. 341, no. 6145, pp. 537–540, 2013.

[12] T.-Y. Cheng, W.-Y. Wang, J.-S. Li, J.-X. Guo, S. Liu, and J.-Q. Lü, "Rotational Doppler effect in vortex light and its applications for detection of the rotational motion," *Photonics*, vol. 9, no. 7, p. 441, Jun. 2022.

[13] S. Qiu, T. Liu, Y. Ding, Z. Liu, L. Chen, and Y. Ren, "Rotational Doppler effect with vortex beams: Fundamental mechanism and technical progress," *Frontiers Phys.*, vol. 10, Jun. 2022, Art. no. 938593.

[14] M. Lavery, S. M. Barnett, F. C. Speirits, and M. J. Padgett, "Observation of the rotational Doppler shift of a white-light, orbital-angular-momentum-carrying beam backscattered from a rotating body," *Optica*, vol. 1, no. 1, pp. 1–4, 2014.

[15] S. Fu, T. Wang, Z. Zhang, Y. Zhai, and C. Gao, "Nondiffractive Bessel–Gauss beams for the detection of rotating object free of obstructions," *Opt. Exp.*, vol. 25, no. 17, pp. 20098–20108, 2017.

[16] A. Q. Anderson, E. F. Strong, B. M. Heffernan, M. E. Siemens, G. B. Rieker, and J. T. Gopinath, "Observation of the rotational Doppler shift with spatially incoherent light," *Opt. Exp.*, vol. 29, no. 3, pp. 4058–4066, 2021.

[17] S. Qiu et al., "Influence of lateral misalignment on the optical rotational Doppler effect," *Appl. Opt.*, vol. 58, no. 10, pp. 2650–2655, 2019.

[18] Z. Zhang, L. Cen, J. D. Zhang, J. Hu, F. Wang, and Y. Zhao, "Rotation velocity detection with orbital angular momentum light spot completely deviated out of the rotation center," *Opt. Exp.*, vol. 28, no. 5, pp. 6859–6867, 2020.

[19] S. Qiu et al., "Rotational Doppler effect detection by LG beams with a nonzero radial index," *Opt. Exp.*, vol. 29, no. 7, pp. 10275–10284, 2021.

[20] J. Deng, K. Li, W. Liu, and G. Li, "Cascaded rotational Doppler effect," *Opt. Lett.*, vol. 44, no. 9, pp. 2346–2349, 2019.

[21] A. S. Ostrovsky, C. Rickenstorff-Parrao, and V. Arrizón, "Generation of the 'perfect' optical vortex using a liquid-crystal spatial light modulator," *Opt. Lett.*, vol. 38, no. 4, pp. 534–536, 2013.

[22] S. Qiu et al., "Spinning object detection based on perfect optical vortex," *Opt. Lasers Eng.*, vol. 124, Jan. 2020, Art. no. 105842.

[23] J. Mendoza-Hernández, M. Hidalgo-Aguirre, A. I. Ladino, and D. Lopez-Mago, "Perfect Laguerre–Gauss beams," *Opt. Lett.*, vol. 45, no. 18, pp. 5197–5200, 2020.

[24] X. Liu, Y. E. Monfared, R. Pan, P. Ma, Y. Cai, and C. Liang, "Experimental realization of scalar and vector perfect Laguerre–Gaussian beams," *Appl. Phys. Lett.*, vol. 119, no. 2, Jul. 2021, Art. no. 021105.

[25] J. Mendoza-Hernández, M. L. Arroyo-Carrasco, M. D. Iturbe-Castillo, and S. Chávez-Cerda, "Laguerre–Gauss beams versus Bessel beams showdown: Peer comparison," *Opt. Lett.*, vol. 40, no. 16, pp. 3739–3742, 2015.

[26] V. Arrizón, U. Ruiz, R. Carrada, and L. A. González, "Pixelated phase computer holograms for the accurate encoding of scalar complex fields," *J. Opt. Soc. Amer. A, Opt. Image Sci.*, vol. 24, no. 11, pp. 3500–3507, 2007.

[27] A. Dudley, G. Milione, R. R. Alfano, and A. Forbes, "All-digital wavefront sensing for structured light beams," *Opt. Exp.*, vol. 22, no. 11, pp. 14031–14040, 2014.

[28] Y. Zhang et al., "Ultrafast multi-target control of tightly focused light fields," *Opto-Electron. Adv.*, vol. 5, no. 3, 2022, Art. no. 210026.

[29] S. Lin et al., "All-optical vectorial control of multistate magnetization through anisotropy-mediated spin-orbit coupling," *Nanophotonics*, vol. 8, no. 12, pp. 2177–2188, Dec. 2019.

[30] Z. Jin et al., "Phyllotaxis-inspired nanosieves with multiplexed orbital angular momentum," *eLight*, vol. 1, no. 1, pp. 1–11, Dec. 2021.

[31] T. P. Purdy, R. W. Peterson, and C. A. Regal, "Observation of radiation pressure shot noise on a macroscopic object," *Science*, vol. 339, no. 6121, pp. 801–804, Feb. 2013.

[32] S. Kawanishi and M. Saruwatari, "A very wide-band frequency response measurement system using optical heterodyne detection," *IEEE Trans. Instrum. Meas.*, vol. 38, no. 2, pp. 569–573, Apr. 1989.

[33] D. Censor, "Theory of the Doppler effect: Fact, fiction and approximation," *Radio Sci.*, vol. 19, no. 4, pp. 1027–1040, Jul. 1984.